



First Principles Calculations of Atomic Nickel Redox Potentials and Dimerization Free Energies: A Study of Metal Nanoparticle Growth

Dian Jiao,[†] Kevin Leung,^{*,‡} Susan B. Rempe,^{*,†} and Tina M. Nenoff[‡]

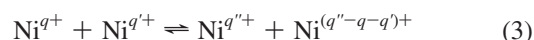
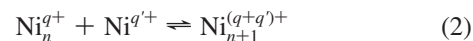
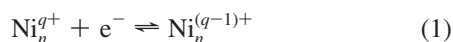
Nanobiology Department, MS 0895, Sandia National Laboratories, Albuquerque, New Mexico 87185, United States, and Surface and Interface Sciences Department, MS 1415, Sandia National Laboratories, Albuquerque, New Mexico 87185, United States

Received August 3, 2010

Abstract: The redox potentials and dimerization free energies of transient transition metal cations in water shed light on the reactivity of species with unusual charge states and are particularly pertinent to understanding the mechanism and feasibility of radiolysis-assisted metal nanoparticle growth from salt solutions. A combination of quasi-chemical theory and *ab initio* molecular dynamics thermodynamic integration methods are applied to calculate these properties for nickel. The reduction potential for Ni²⁺ (aq) is predicted to be between −1.05 to −1.28 V, which is substantially lower than previous estimates. This suggests that Ni²⁺ reduction may possibly occur in the presence of organic radical anion electron scavengers and hydrogen atoms, not just hydrated electrons. In contrast, Ni⁺ is found to be stable against disproportionation. The formation of dimers Ni₂ and Ni₂⁺ from Ni and Ni⁺ are predicted to be favorable in water.

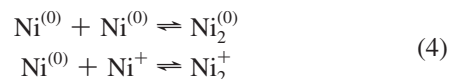
I. Introduction

Accurate modeling of reduction–oxidation (redox) reactions are pertinent to a wide range of electrochemical applications including batteries,¹ metal extraction,² catalysis,³ and biology.^{4,5} In particular, short-lived transition ionic metal species with unusual charge states are important intermediates in many multistep, multielectron processes. An intriguing application is the radiolysis-assisted synthesis of metal nanoparticles and alloys in aqueous solutions.^{6–11} Secondary electrons from γ radiation or other sources can directly or indirectly (through electron-scavenging organic radical anions) reduce metal ions in salt solutions to their low oxidation states. Metal clusters are then formed via a series of reduction, clustering, and disproportionation reactions:^{12–15}



The choice of the Ni example allows us to support recent γ -irradiation experiments.^{7,8} Not indicated in eqs 1–3 is the possibility of mixed alloy formation involving more than one metal element. In fact, the synthesis of unique alloys that are not thermodynamically stable can be accomplished via this route.^{7,8}

The properties of transient metal species in water are difficult to measure. In this work, we use modeling techniques to investigate the initial stages of radiolysis-assisted Ni cluster formation demonstrated in experiments. The free energy change of clustering (eq 2) governs nanoparticle growth. The clustering of transition metal atoms is important to catalysis and has been extensively studied,^{16–19} but the nucleation process has seldom been modeled in aqueous media. As a first step, we compute the dimerization free energies of Ni in water:



* Corresponding author e-mails: slrempe@sandia.gov (S.B.R.), kleung@sandia.gov (K.L.).

[†] Nanobiology Department.

[‡] Surface and Interface Sciences Department.

Such clustering reactions have been measured for Ag,^{20,21} but to our knowledge not the transition metal element Ni. Detailed studies of gas-phase, unhydrated Ni dimers have revealed much complexity.^{22–29} Our work builds on these past studies but focuses on the interaction between the neutral and cationic monomers and dimers with liquid water. As will be shown, the formation of $\text{Ni}_2^{(0)}$ and Ni_2^{q+} dimers are found to be favorable, and they represent the first steps of the complex mechanism in the formation of Ni nanoclusters from aqueous salt solutions.

We also consider another significant property that can benefit from theoretical input, namely, the redox potentials (Φ_{redox}) associated with transient Ni^{q+} and Ni_2^{q+} species. Φ_{redox} plays a crucial role in determining what cluster size, stoichiometry, and net charge can exist under experimental conditions. As discussed in pioneering work on the radiolysis synthesis of Au, Ag, and bimetallic Au/Ag nanoclusters,^{30,31} the detailed mechanism of cluster formation depends on the redox potentials of the metal salts in solution, in our case Ni_n^{q+} (eq 1) and analogous bimetallic species relative to the reducing species (excess electrons and organic radical anions) that exist in the γ -irradiated solution. The excess electron chemical potential in liquid water is generally listed at -2.7 to -2.9 V relative to the standard hydrogen electrode (SHE),^{32,33} while electron-scavenging hydroxymethyl radical anions present in radiolysis experiments are at a more modest -1.18 V.⁷ For Ni_n^{q+} to be reduced in solution, it must exhibit a more positive Φ_{redox} than the relevant redox potential of the electron-donating species.

Φ_{redox} can be rigorously separated into two contributions: the change in standard state ion hydration free energy (ΔG_{hyd}) and the ionization potential (IP). Φ_{redox} is referenced to the SHE by subtracting 4.44 V. In the literature, the reported Φ_{redox} of transient first row transition metal ions in water often contain theoretical components. Thus, using experimental IP and Ni^+ and Ni^{2+} ΔG_{hyd} values estimated via Pauling radius interpolation and the Born hydration free energy formula,³⁴ respectively, Baxendale and co-workers^{13,14} have reported a -2.7 V Φ_{redox} for $\text{Ni}^{2+} + \text{e}^- \rightleftharpoons \text{Ni}^+$. This Φ_{redox} is very close to that of the electron injected into water,^{32,33} suggesting that hydrated electrons are marginally sufficient to reduce Ni^{2+} . At the -1.18 V associated with organic radical anions found under radiolysis conditions,⁷ Ni^{2+} should be inert. Baxendale et al. have, however, ignored the ligand-field splitting induced energetic stabilization arising from the first hydration shell water molecules, which can amount to a significant fraction of an electronvolt for first row transition metal ions.³⁵ As will be shown, our predictions lead to a substantial revision of this earlier estimate.¹³

Two modern computational strategies have been applied to calculate ΔG_{hyd} . In the more widely used approach, the Density Functional Theory (DFT) electronic structure method is used to optimize the geometry of gas-phase clusters of transition metal ions containing first hydration shell water molecules.^{36–42} DFT explicitly takes into account ligand field splittings. The outer shell water molecules can be represented explicitly or by an implicit solvent model via a dielectric continuum approximation.^{40,42} A successful implementation

of this solvation method³⁵ is the “quasi-chemical theory” (QCT).^{43–46} This method makes use of the most probable distribution of hydration numbers (i.e., the number of water molecules, N_w , residing in the ionic hydration shell). The predicted equilibrium hydration number can be compared with X-ray and neutron scattering data and is complementary to nuclear magnetic resonance relaxation time information.⁴⁷

A second approach applies *ab initio* molecular dynamics (AIMD) simulations, where metal ions and all water molecules, including outer-shell ones, are treated explicitly using DFT at each finite temperature molecular dynamics time step.^{48–51} Thermodynamic integration⁵² (TI) using AIMD simulations have yielded hydration free energies for simple ions in good agreement with experiments,^{53,54} suggesting that reliable Φ_{redox} can also be predicted with the AIMD method provided an accurate IP can be obtained theoretically or experimentally.

The two theoretical methods complement each other. The QCT approach directly computes the hydration free energy of any species, divided into contributions that provide insights into the effects from local and distant solvent. Past work attests to the success of this approach in calculating hydration free energies of small molecules.^{35,43,44,55} The approach has also been used to investigate mechanisms of selectivity in biological ion binding sites.^{56,57} The more costly AIMD method can generate new insights into the bulk solvation structures of low-valence transition metals, which are of basic scientific interest due to their unusual electronic properties.^{50,58–61} For transition metal elements, AIMD readily yields differences in ΔG_{hyd} between different ionic charge states, but not the ΔG_{hyd} themselves. A comparison between AIMD and QCT ΔG_{hyd} changes as reduction reactions occur allows critical examination of the different approximations used in both approaches and helps elucidate the discrepancies between theoretical and experimental Φ_{redox} reported in the literature.^{37–39,41}

Treatment of the transition metal ion d electrons is efficiently improved using DFT+U (Hubbard-like) augmentations^{62,63} within AIMD simulations, which has been applied to molecular systems.⁶⁴ QCT has the advantage of being much more computationally efficient and permits the use of hybrid DFT functionals, which are generally more accurate than non-Hubbard augmented, nonhybrid DFT functionals for the properties of main group elements and many transition metal complexes. The coupled-cluster (CCSD(T)) level of theory, more reliable than hybrid functionals, can also be applied to calculate gas-phase binding energies and calibrate DFT results.

Here, we have applied first principles methods and the theoretical frameworks described above to calculate the redox potentials and dimerization free energies of monomeric and dimeric nickel species in liquid water. In the following parts of this paper, section II details the AIMD and QCT methods used. Section III describes the computational results, and section IV concludes the paper with brief discussions.

II. Method

II.A. Hydration Calculation by QCT. The quasi-chemical theory enables calculation of the hydration free energy in terms of individual contributions from inner-shell and outer-shell solvent domains. The inner-shell domain typically consists of the ion and water molecules that form the first hydration shell. The binding free energy for the formation of inner-shell complexes can be computed in the absence of outer-shell solvent as

$$\Delta G^{(0)} = G_{\text{Ni}^{q+}(\text{H}_2\text{O})_n}^{(0)} - G_{\text{Ni}^{q+}}^{(0)} - nG_{\text{H}_2\text{O}}^{(0)} \quad (5)$$

The equilibrated structures of nickel–water clusters, which represent the inner hydration shell regions, are optimized using DFT methods starting from AIMD simulation configurations. QCT DFT calculations are performed using the Gaussian suite of programs.⁶⁵ Frequencies and zero-point energies are determined using CCSD(T)⁶⁶ and the Becke-3-parameter-Lee–Yang–Parr (B3LYP) functional.⁶⁷ Some results for the Perdew–Burke–Ernzerhof (PBE) functional⁶⁸ are also found in the Supporting Information document (SI). The 6-311+G(d,p) basis set is applied throughout. Standard, finite temperature and zero point energy contributions are added to ΔG^0 . The optimal spin state is chosen as the most stable state.

Free energy contributions from the outer region consist of the molecular packing contribution (cavity) and the interactions between the inner-shell cluster and outer-shell solvent molecules. Since AIMD calculations do not take into account the small cavity contribution, this term is left out from the QCT calculation for the sake of better comparison with AIMD. The solvation effects from the outer region are obtained by treating the external solvent as a dielectric continuum. The electrostatic potential is evaluated by solving the Poisson–Boltzmann equation with the APBS package.⁷² The numerical technique used to solve the equation is a combination of the standard finite difference focusing method and the parallel adaptive finite element algorithm.⁷³ For the APBS calculation, partial charges on an inner-shell complex are acquired from the ChelpG method with the 6-311+G(d,p) basis set, while the radii for oxygen and hydrogen atoms are taken from the literature.⁶⁹ Radii of nickel ions used to define the division between inner and outer solvent domains are determined by the first minima in ion–oxygen pairwise correlation functions, $g(r)$, from AIMD simulations. Where experimental data is available (e.g., Ni^{2+}), the simulated minima match results from X-ray experiments.^{70,71} The fine mesh domain length is set to 10 Å and the coarse mesh domain length, 30 Å. The dielectric constants for the inner and outer shells are set to 1.0 and 78.5, respectively.

II.B. AIMD Simulations. Spin-polarized AIMD simulations apply the Vienna *ab initio* simulation program (VASP),⁷⁴ projected-augmented wave (PAW) pseudopotentials^{75,76} (PP) with only valence electrons for H and O atoms, and a Ni PP that includes pseudovalent 3p electrons, the PBE functional,⁶⁸ Γ -point Brillouin zone sampling, and a 400 eV plane-wave energy cutoff.

Semilocal functionals such as PBE are generally inadequate for treating first row transition metal complexes,⁷⁷

even while they can be successful with dimers in the gas phase.⁷⁸ As will be shown, the B3LYP functional is more accurate for depicting interactions of Ni species with water. Since the hybrid functional B3LYP is too costly to use in AIMD settings, we apply the DFT+U approach⁶² to Ni 3d orbitals only. The U value is fitted to reflect the zero temperature B3LYP binding energy in the $\text{Ni}^{2+}(\text{H}_2\text{O})_6$ cluster. AIMD trajectories for $q \leq 1$ are generated using the PBE functional, whereas $\text{Ni}^{q+}(\text{aq})$ trajectories for $q \geq 1$, taken from ref 53, are generated using the DFT+ U functional with $U = 4$ eV. Fitting VASP to Gaussian results is possible because, at $T = 0$ K, PBE geometry optimization calculations that apply VASP PAW pseudopotentials and the plane-wave basis and those that apply the Gaussian suite of codes and the 6-311+G(d,p) basis⁶⁵ yield $\text{Ni}^{2+}(\text{H}_2\text{O})_6$ binding energies that agree to within a few tenths of an electronvolt. While using two types of functionals to generate AIMD trajectories is admittedly awkward, the hydration free energies should not be strongly affected. As discussed in ref 53, the hydration structures of most Ni species are sufficiently similar for the PBE and DFT+ U methods, so that using either to generate trajectories should yield very similar ΔG_{hyd} values. An estimate of the small error introduced in using AIMD/PBE trajectories will be discussed in the Results section and in the SI. (In contrast, DFT+ U and PBE predict ligand field splittings and reaction energies that differ by fractions of an electronvolt.) PBE is selected to generate trajectories in this work because, for the $\text{Ni}_2^{2+}(\text{aq})$ species only, it gives stable structures, while B3LYP does not (see below).

A Nose thermostat fixes the temperature at $T = 400$ K, which is needed for the PBE functional to describe the room temperature experimental liquid water structure.⁷⁹ The deuterium mass is adopted for all protons to allow a larger time step while the H mass is assumed whenever water density is reported. Along with Born–Oppenheimer dynamics time steps of 0.25 fs and a 10^{-6} eV energy convergence criterion, these settings limit the temperature drifts to 1 K/ps. The trajectory length is 30 ps for each of the TI windows. Initial configurations are pre-equilibrated using the extended simple point charge (SPC/E) water model⁸⁰ and a Ni^{q+} force field consisting of a $+q$ point-charge scaled to the net charge of the corresponding AIMD simulation cell plus a Lennard–Jones functional form. Such crude force fields do not yield the well-structured first hydration shells of transition metal ions but are useful for dielectric relaxation of outer-shell water molecules that accompany changes in ionic charges. After switching from force fields to AIMD simulations, we find that the distinctive Ni^{q+} first hydration shell generally becomes equilibrated and yields the expected structures within 2 ps, except for $\text{Ni}_2^{(0)}$, which takes 7 ps to reach the equilibrium hydration number (N_w). The short equilibration time suggests that AIMD predicted free energy changes should not depend on initial conditions.

AIMD simulations for a single Ni^{q+} ion, $0 \leq q \leq 2$, are performed using $9.885 \times 9.885 \times 9.885$ Å³ simulation cells that contain a Ni atom/ion and 32 H₂O molecules. In the case of the dimer, the $12.885 \times 9.885 \times 9.885$ Å³ cells contain a Ni dimer and 40 water molecules, with the x and

y coordinates of both Ni atoms held fixed and identical along the long axis of the simulation cell.

II.C. Hydration Free Energy Changes via Thermodynamic Integration. To calculate differences in hydration free energy, $\Delta\Delta G_{\text{hyd}}$, between species in different charge states (q_i and q_f) using AIMD simulations, thermodynamic integration (TI)^{52,81} was performed via

$$\Delta\Delta G_{\text{H}_{\text{yd}}} = \int_{q_i}^{q_f} \langle dH(\lambda)/d\lambda \rangle_{\lambda} d\lambda + (q_f - q_i)\Delta\phi \quad (6)$$

Here, $H(q)$ is the total potential energy of the simulation cell at a net charge $\lambda = q$ in the simulation cell computed using a modified version of VASP,⁸² minus the energy of the isolated Ni^{q+} with the same spin state. In VASP simulations, q is set by imposing a fixed number of electrons (which can be a noninteger) in the simulation cell. This is appropriate for modeling hydrated $\text{Ni}^{(0)}$, Ni^+ , Ni^{2+} , and the intermediate charges bracketed by these species because the fractional electron is found to reside on the Ni 3d orbitals via maximally localized Wannier functional analysis.⁸⁵ The one exception to this rule will be discussed in section III.D. The net spin is tuned to a value linearly interpolated between the stable spin state of the end points of the TI simulation in the aqueous phase, *not* necessarily those of the stable spin states of the gas-phase Ni species. This procedure captures the net hydration free energy, including the ligand field splitting, to be discussed in more detail in section III.C. It excludes the gas-phase ionization potential contribution, which tends not to be predicted accurately from widely used DFT functionals. The IP value is taken from experiments whenever possible. If the stable spin states of the bare and hydrated Ni species differ, as is the case with $\text{Ni}^{(0)}$, a spin-flip energy is added post processing to the change in hydration free energy.

Also included in $H(q)$ are monopole- and image charge-induced electrostatic corrections due to the periodic boundary conditions,⁸³ $\Delta E_{\text{Ewald}} = q^2/(2\alpha\epsilon_0 L)$, where α is the Madelung constant, L is the cubic cell size dimension, and ϵ_0 is the pertinent dielectric constant. ϵ_0 is set to unity for isolated ions and to infinity for water. Another, much smaller finite size correction, the change in $\Delta E_{\text{quad}} = 2\pi q^2 R^2/3L^3$, where R is the ion radius, is added to $\Delta\Delta G_{\text{hyd}}$ post processing.⁸⁴ With our simulation cell size and an estimated $R = 2 \text{ \AA}$ for Ni^{q+} , which reflects the approximate position of the peaks in $g(r)$ (Figures 1 and 2), ΔE_{quad} amounts to 0.125 and 0.500 eV for $q = 1$ and 2, respectively.

Operationally, at every 0.1 ps interval, we use finite difference to sample $dH(q)/dq \approx [H(q_+) - H(q_-)]/(le/20)$, $q_{\pm} = q \pm le/40$, at the fixed atomic configurations in the snapshot. When q is an integer, q_{\pm} values are shifted so that they do not exceed the boundary values of the electron addition half-cell reaction. A six-point trapezoidal rule integrates over the resulting $\langle dH(q)/dq \rangle_q$. Equation 6 is rigorous even for models with electronic polarizability.

Surface potentials ($\Delta\phi$) at fluid–fluid and fluid–solid interfaces contribute to solvation free energies. In particular, the air–water surface potential is an integral part of the ion hydration free energy ΔG_{hyd} via the second term, $(q_f - q_i)\Delta\phi$, in eq 6.⁸⁶ $\Delta\phi$ can be decomposed into dipolar ($\Delta\phi_d$) and quadrupolar ($\Delta\phi_q$) contributions.⁸⁶ $\Delta\phi_q$ is a bulk liquid water

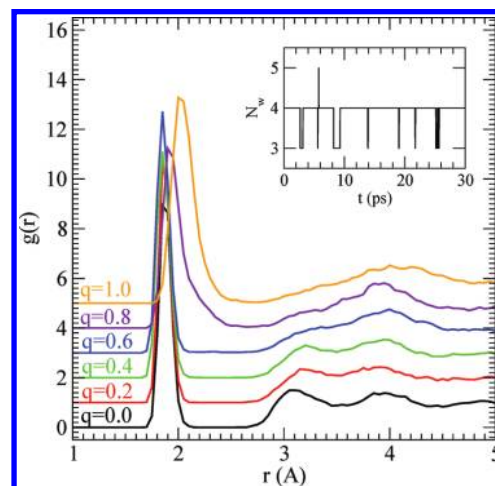


Figure 1. AIMD pair correlation function $g(r)$ between O_w and Ni^{q+} as q varies. Black, red, green, blue, violet, and orange lines denote $q = 0.0, 0.2, 0.4, 0.6, 0.8$, and 1.0 , respectively, offset by one density unit along the y axis. $N_w = 2.00, 2.00, 2.03, 2.06, 2.86$, and 3.93 for these Ni^{q+} species, respectively. The inset depicts instantaneous N_w for $q = 1.0$.

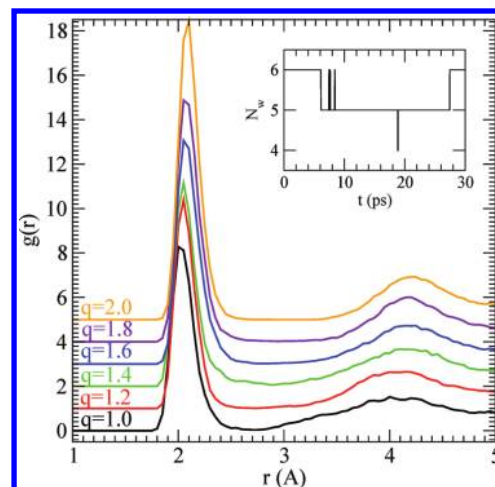


Figure 2. AIMD pair correlation function $g(r)$ between O_w and Ni^{q+} as q varies. Black, red, green, blue, violet, and orange lines denote $q = 1.0, 1.2, 1.4, 1.6, 1.8$, and 2.0 , respectively. $N_w = 3.81, 4.34, 4.80, 5.17, 5.48$, and 6.00 for these q values, respectively. The inset depicts the instantaneous N_w for $q = 1.8$ (black).

quantity independent of the nature of interfaces, and the theoretical $\Delta\phi_q$ value has been estimated using the PBE quadrupole component at 1.0 g/cm^3 water density.^{53,87} For $\Delta\phi_d$, we note that this work seeks to mimic electrochemical measurements of electron transfer between a metal electrode and Ni^{q+} species in water. To our knowledge, the pertinent water–electrode $\Delta\phi_d$ has not been computed using atomic simulations. The infinite dielectric constant of metal, which leads to “image charges” inside the metal,⁸⁸ should partly compensate for the potential drop due to water surface dipoles. It should be a reasonable assumption that the water–metal electrode ϕ_d is smaller in magnitude than the air–water ϕ_d . Thus, we have omitted $\Delta\phi_d$ in our $\Delta\Delta G_{\text{hyd}}$ calculation. This argument is not completely rigorous because both $\Delta\phi_d$ and $\Delta\phi_q$ depend on the choice of molecular center; only $\Delta\phi$ is independent of such choices. Nevertheless, from

the image-charge argument, the ambiguity in redox potential introduced from omitting ϕ_d should be less than the 0.21 V associated with vapor-water $\Delta\phi_d$ for the SPC/E water model. Both Baxendale et al.'s estimates^{13,14} and the QCT approach (see below) exclude the surface potential.

III. Results

III.A. Choice of DFT Functional and Method. First, we describe the benchmarking procedure that informs our choice of DFT functional. The gas-phase $\text{Ni}^{(0)}(\text{H}_2\text{O})_2$ cluster is sufficiently small so that the more reliable quantum chemistry CCSD(T) method can be used to perform single point binding energy calculations to calibrate DFT results. PBE, B3LYP, and CCSD(T) predict an ΔE_{bind} of 1.88, 1.06, and 1.28 eV, respectively, for this complex. This test suggests that B3LYP is more reliable than PBE for $\text{Ni}^{(0)}$ hydration.

PBE and B3LYP predict 16.31 and 15.71 eV binding energies for the gas-phase $\text{Ni}^{2+}(\text{H}_2\text{O})_6$ cluster. The 0.60 eV discrepancy is mostly due to differences in energies from ligand field splitting, which was estimated in ref 35 as follows. The QCT/B3LYP ΔG_{hyd} values are computed for Ca^{2+} and Zn^{2+} , which contain either an empty or a full 3d shell and therefore do not exhibit ligand field splitting. Interpolating between these extremes and examining the deviation of individual transition metal ions as a function of 3d orbital occupation leads to a 1.3 eV ligand-field stabilization for Ni^{2+} in water. We have reproduced a similar result by considering only the B3LYP gas-phase $\text{M}^{2+}(\text{H}_2\text{O})_6$ energy at $T = 0$ K, excluding zero-point corrections, outer-shell water contributions, and thermal effects. We conclude that gas-phase $\text{Ni}^{2+}(\text{H}_2\text{O})_6$ is stabilized by 1.40 eV relative to the value interpolated between Ca^{2+} and Zn^{2+} . Using this gas-phase route, the PBE functional yields a 1.80 eV ligand-field stabilization energy for Ni^{2+} . The B3LYP ligand-field splitting is in better agreement with the 1.26 eV spectroscopic data^{35,89} than the PBE one. Thus, B3LYP should be considered more accurate for Ni^{2+} hydration.

PBE and B3LYP binding energies for gas-phase $\text{Ni}^+(\text{H}_2\text{O})_4$ also differ by 0.48 eV. An effort to interpolate ligand-field stabilization for the $\text{Ni}^+(\text{H}_2\text{O})_4$ complex fails. While $\text{K}^+(\text{H}_2\text{O})_4$, devoid of 3d electrons, is stable in the gas phase, $\text{Cu}^+(\text{H}_2\text{O})_4$, the hydrated species, which could have fully occupied 3d orbitals and no 4s electrons, collapses. This complex turns into a linear, two-coordinated Cu with the two other water molecules relegated to the outer shell and linked to the two inner shell H_2O 's through hydrogen bonds. The linear structure is consistent with previous AIMD simulations of hydrated Cu^+ .⁵⁹

Despite lacking an estimate of ligand-field stabilization energy for $\text{Ni}^+(\text{H}_2\text{O})_4$ to validate PBE and B3LYP binding energies, we can test binding between water and neutral and divalent nickel atoms. PBE is shown to substantially overestimate the binding between water and both $\text{Ni}^{(0)}$ and Ni^{2+} . Thus, in the remainder of this manuscript, we focus on two complementary methods, QCT/B3LYP and AIMD/DFT+ U with the Hubbard U value fitted to the B3LYP $\text{Ni}^{2+}(\text{H}_2\text{O})_6$ binding energy.

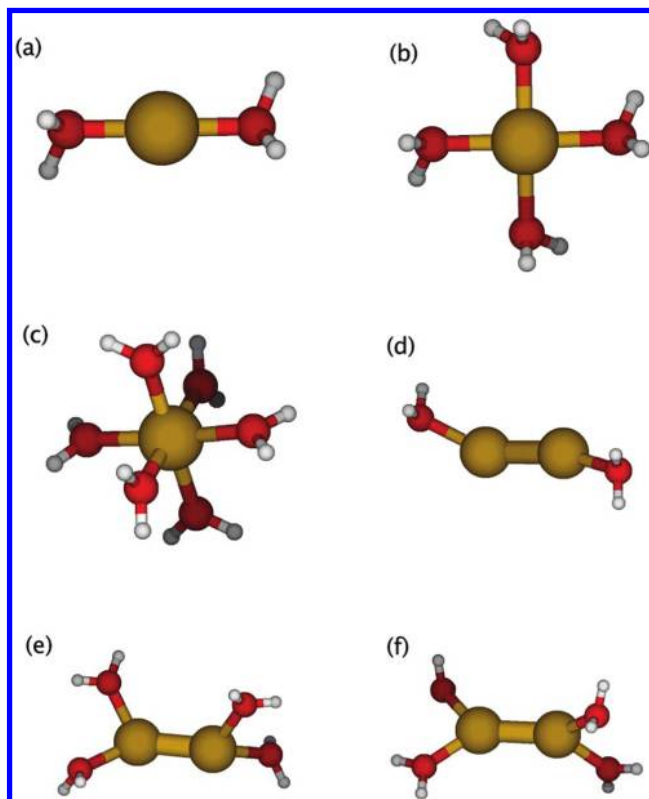


Figure 3. Optimized gas-phase clusters using the Gaussian code and B3LYP/6-311+G(d,p) level of theory. (a) $\text{Ni}^{(0)}(\text{H}_2\text{O})_2$ ($s = 0$); (b) $\text{Ni}^+(\text{H}_2\text{O})_4$ ($s = 1/2$); (c) $\text{Ni}^{2+}(\text{H}_2\text{O})_6$ ($s = 1$); (d) $\text{Ni}_2^{(0)}(\text{H}_2\text{O})_2$ ($s = 1$); (e) $\text{Ni}_2^+(\text{H}_2\text{O})_4$ ($s = 3/2$); (f) $\text{Ni}_2^+(\text{H}_2\text{O})_4$ ($s = 1/2$). Blue, red, and white spheres represent Ni, O, and H atoms, respectively.

III.B. Hydration Structures. Figures 1 and 2 depict the pair correlation functions, $g(r)$, between Ni^{q+} and the water oxygen (O_w) site. Only integral values of q are physical, but the fractional q results, needed for TI calculations, reveal interesting trends in the hydration structure. Also listed in the figure captions are the hydration numbers, N_w , defined as the spatial integral up to the first minimum ($r = 2.6$ Å) in $g(r)$.

While the bare Ni atom is a spin triplet ($s = 1$), both B3LYP and DFT+ U predict that $\text{Ni}^{(0)}(\text{H}_2\text{O})_2$ is most stable in the singlet state ($s = 0$) in the gas phase. (See the SI for more spin state information.) The $g(r)$ between singlet $\text{Ni}^{(0)}$ and the oxygen site of water molecules obtained in AIMD simulations exhibits a sharp first peak at $R_{\text{Ni-O}} = 1.8$ Å that integrates to two H_2O molecules. The instantaneous hydration configuration in liquid water is linear, similar to the gas-phase optimized structure shown in Figure 3a, which in turn resembles that of $\text{Cu}^+(\text{H}_2\text{O})_2$.⁵⁹ The sharp first peak reflects strong covalent bonds between water and $\text{Ni}^{(0)}$. As q increases from 0.0 to 1.0, the first peak in $g(r)$ broadens and shifts to a larger distance of $r = 2.0$ Å. This is presumably because more water molecules enter the hydration shell at larger q . The increased repulsion between the oxygen sites of the first shell hydration H_2O molecules should weaken the interaction between each individual H_2O and the Ni^{q+} . At $q = 1.0$, the number of H_2O molecules in the first hydration shell increases to 3.8 and a stable square planar hydration shell is formed, just like the gas-phase $\text{Ni}^+(\text{H}_2\text{O})_4$

complex (Figure 3b). The secondary structure in $g(r)$ at $r = 3.1$ Å, clearly discernible at $q = 0$, also becomes smeared out at larger q and disappears beyond $q = 0.4$.

Ni^+ is in the doublet ($s = 1/2$) spin state with this ligand field. The inset to Figure 1 depicts the temporal fluctuations in N_w at $q = 1.0$, showing that the water molecules enter and leave the first hydration shell on a sub-picosecond time scale despite the stable hydration structure. Two of the H_2O molecules initially residing in the hydration shell have been replaced by H_2O molecules from the outlying regions by the end of this 30 ps trajectory.

As q further increases from 1 to 2 (see Figure 2), N_w smoothly rises from 4 to 6. The first peak position in $g(r)$ remains at $r \approx 2.1$ Å but sharpens as q approaches 2, at which point the well-known Ni^{2+} octahedral first hydration shell³⁵ (Figure 3c) is observed in AIMD simulations. Fluctuations of instantaneous N_w also occur on sub-picosecond time scales for $q < 2$ except at $q = 1.8$, where transition between 5- and 6-fold coordination occurs more slowly (inset to Figure 2).

Turning our attention to the dimers, $\text{Ni}_2^{(0)}$ is predicted to be a spin triplet with all DFT methods we have considered. In AIMD simulations of this species in water, the Ni atoms collectively exhibit $N_w = 3$; one Ni is typically instantaneously coordinated to two H_2O molecules and the other to one H_2O . In the gas phase, two-coordinated $\text{Ni}_2^{(0)}(\text{H}_2\text{O})_2$ forms a stable linear cluster (Figure 3d). However, three-coordinated $\text{Ni}_2^{(0)}(\text{H}_2\text{O})_3$ is not stable; one of the H_2O molecules migrates to the outer shell, forming a hydrogen bond with one of the two remaining H_2O 's directly coordinated to Ni. Thus, for QCT/B3LYP calculations, we focus on the two-coordinated $\text{Ni}_2^{(0)}$.

For the Ni_2^+ cation dimer, the B3LYP functional predicts that the quartet ($s = 3/2$) state is more stable than the doublet ($s = 1/2$) with and without dielectric continuum treatment of outer-shell water. Two H_2O molecules are coordinated to each Ni of the $\text{Ni}_2^+(\text{H}_2\text{O})_4$ complex. The two Ni atoms exhibit similar $\text{O}_w\text{--Ni--O}_w$ angles (Figure 3e) and equal net integrated charge and spin densities according to Mulliken analysis.⁹⁰ Figure 4 depicts the $g(r)$ between Ni and O_w for quartet Ni_2^+ .

For completeness, we also briefly discuss the doublet $\text{Ni}_2^+(\text{H}_2\text{O})_4$ cluster, which is metastable in the gas phase. The two Ni atoms are in manifestly different chemical bonding environments (Figure 3f). Mulliken analysis reveals that one Ni has a large net charge and spin density, and appropriately the two coordinating water molecules are at 90° to each other as in a square-planar $\text{Ni}^+(\text{H}_2\text{O})_4$ complex. The other Ni is charge neutral, has little or no spin density, and the two H_2O 's are indeed at 180° from each other as in the linear $\text{Ni}^{(0)}(\text{H}_2\text{O})_2$ complex. Such solvent-induced asymmetry in charge distribution has been examined in I_3^- and other systems.⁹¹ This low-spin cluster will not be the subject of AIMD free energy calculations.

$\text{Ni}_2^{2+}(\text{H}_2\text{O})_n$ gas-phase complexes are unstable within the B3LYP treatment; the two Ni^{2+} 's become separated by a water molecule during geometry optimization. In contrast, in PBE calculations, the Ni–Ni bond does not spontaneously break in $\text{Ni}_2^{2+}(\text{H}_2\text{O})_5$. Consistent with this gas-phase predic-

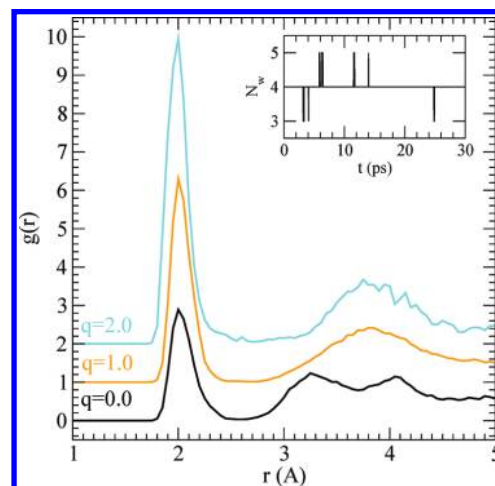


Figure 4. $g(r)$ between O_w and the Ni sites for Ni_2^{q+} as q varies. Black, orange, and cyan lines denote $q = 0.0$, 1.0, and 2.0, respectively. $N_w = 3.00$, 4.01, and 5.22 for the two Ni atoms combined. The inset depicts instantaneous N_w for $q = 1.0$.

tion, the Ni_2^{2+} complex is stable in AIMD/PBE simulations. Recall this is the reason we choose to run AIMD simulations with the PBE functional and then perform DFT+ U calculations for the hydration free energy calculations based on PBE configurations. The two Ni's in Ni_2^{2+} yield a combined $N_w = 5.22$. Individually, each Ni is found to exhibit $N_w \approx 3$; thus on average, one H_2O is shared between the two Ni, simultaneously within the hydration shell of both. This sharing does not occur for $\text{Ni}_2^{(0)}$ and Ni_2^+ but is indeed observed in the gas-phase $\text{Ni}_2^{2+}(\text{H}_2\text{O})_5$ optimized geometry (not shown). Mulliken analysis shows that both Ni ions in this cluster have equal integrated charge and spin densities. Since the covalently bonded Ni_2^{2+} dimer is only stable in water when using the PBE functional, it is likely only marginally stable, and its redox properties will not be the subject of this work.

The hydration number predictions from AIMD simulations for Ni^{q+} and Ni_2^{q+} species are used to determine the number of water molecules used in gas-phase cluster calculations on which the QCT method is based.

III.C. QCT Hydration Free Energies. The components of the QCT absolute hydration free energies for $\text{Ni}^{(0)}$, Ni^+ , and Ni^{2+} are listed in Table 1. It is worth noting that the cavitation energy is not included. However, we estimate the packing contribution to the solvation based on the volume of the cavity. The work that is done to create a cavity by solvating the ion is 0.06, 0.15, and 0.13 eV for $\text{Ni}^{(0)}$, Ni^+ , and Ni^{2+} , respectively, which is insignificant in comparison to the total hydration free energy. The absolute $\Delta G_{\text{hyd}} = -20.59$ eV calculated using the B3LYP functional for Ni^{2+} hydration is in reasonable agreement with experiments (-20.79 eV)⁹² and the prediction in ref 35 using similar methods (-20.49 eV). QCT/B3LYP predicts $\Delta G_{\text{hyd}} = -5.81$ for Ni^+ . Obviously, with the increment of the net charge to higher values, the hydration free energy increases to more negative values. By comparison, Dixon and Baxendale¹³ adopted ΔG_{hyd} values of -4.90 and -21.39 eV for Ni^+ and Ni^{2+} , which are significantly different from the QCT/B3LYP results.

Table 1. Hydration Free Energies of Nickel Species Calculated Using QCT/B3LYP at $T = 300$ K, except That the Asterisk Indicates a CCSD(T) Calculation^a

reactions	$\Delta G^{(0)}$	ΔG	$\Delta\mu$	ΔG_{hyd}
$\text{Ni}^{(0)} + 2\text{H}_2\text{O} \rightleftharpoons \text{Ni}^{(0)}(\text{H}_2\text{O})_2$	-0.217	-0.588	0.163	-0.425
* $\text{Ni}^{(0)} + 2\text{H}_2\text{O} \rightleftharpoons \text{Ni}^{(0)}(\text{H}_2\text{O})_2$	-0.403	-0.774	0.210	-0.564
$\text{Ni}^+ + 4\text{H}_2\text{O} \rightleftharpoons \text{Ni}^+(\text{H}_2\text{O})_4$	-3.757	-4.497	-1.310	-5.807
$\text{Ni}^{2+} + 6\text{H}_2\text{O} \rightleftharpoons \text{Ni}^{2+}(\text{H}_2\text{O})_6$	-12.819	-13.930	-6.658	-20.588
$\text{Ni}_2^{(0)} + 2\text{H}_2\text{O} \rightleftharpoons \text{Ni}_2^{(0)}(\text{H}_2\text{O})_2$	-0.677	-1.047	0.129	-0.919
$\text{Ni}_2^+ + 4\text{H}_2\text{O} \rightleftharpoons \text{Ni}_2^+(\text{H}_2\text{O})_4$ ($s = 3/2$)	-3.463	-4.203	-1.139	-5.342
$\text{Ni}_2^{2+} + 4\text{H}_2\text{O} \rightleftharpoons \text{Ni}_2^{2+}(\text{H}_2\text{O})_4$ ($s = 1/2$)	-3.006	-3.746	-1.132	-4.878
H_2O				-0.361

^a $\Delta G^{(0)}$ is the free energy change for formation of inner-shell clusters in the absence of the surrounding medium. $\Delta G = \Delta G^{(0)} - nRT \ln(1354)$ is the free energy change accounting for the actual density of water. $\Delta\mu$ is the electrostatic interaction between clusters in the inner shell and the implicit solvent in the outer shell. Combining these contributions yields ΔG_{hyd} , the standard state hydration free energy of the Ni_n^{q+} species. Hydration free energy of the water molecule estimated using partial charges from CCSD(T) is -0.390 eV. All values are given in electronvolts.

Table 2. Hydration Free Energy Differences between Nickel Species in Different Charge States ($\Delta\Delta G_{\text{hyd}}$, in eV) and Redox Potentials (Φ_{redox} , volt) Estimated by QCT and AIMD^a

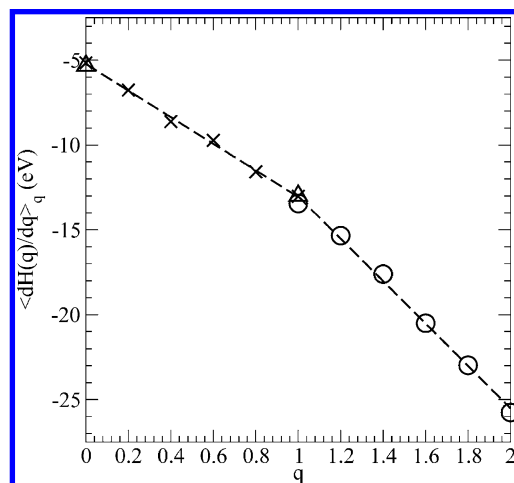
	method	functional	$\Delta\Delta G_{\text{hyd}}$	Φ_{redox}
$\text{Ni}^+ \rightleftharpoons \text{Ni}^{(0)}$	QCT	B3LYP	5.38	-2.18
$\text{Ni}^+ \rightleftharpoons \text{Ni}^{(0)}$	AIMD	DFT+ U	5.37	-2.17
$\text{Ni}^{2+} \rightleftharpoons \text{Ni}^+$	QCT	B3LYP	14.78	-1.05
$\text{Ni}^{2+} \rightleftharpoons \text{Ni}^+$	AIMD	DFT+ U	15.01	-1.28
$\text{Ni}_2^{2+} \rightleftharpoons \text{Ni}_2^{(0)}$	QCT	B3LYP	4.42	-1.44

^a $\Phi_{\text{redox}} = (-\Delta\Delta G_{\text{hyd}}/e) + \text{IP} - 4.44$ volt. The IP for Ni, Ni^+ , and Ni_2 is 7.640, 18.170, and 7.420 eV, respectively. The AIMD $\Delta\Delta G_{\text{hyd}}$'s for Ni^+ and Ni_2^{2+} exhibit standard deviations of 0.02 and 0.04 eV (0.5 and 1.0 kcal/mol), respectively.

The QCT/B3LYP method predicts $\Delta G_{\text{hyd}} = -0.43$ eV for $\text{Ni}^{(0)}$. The QCT/CCSD(T) method gives a similar result for $\text{Ni}^{(0)}$, $\Delta G_{\text{hyd}} = -0.56$ eV. Of all of the charge states, only the solvation of Ni^{2+} has been experimentally documented; other species have only a transient existence. Although carrying zero charge, the neutral Ni monomer and dimer both have significantly favorable solvation in water. Thus, unlike the noble Ag atom dispersed in water,⁵³ reactive transition metal atoms like Ni cannot be described as inert Lennard-Jones spheres.

III.D. Hydration Free Energy Changes upon Reduction. Table 2 depicts the difference in hydration free energies ($\Delta\Delta G_{\text{hyd}}$) between species differing by one electron. Note that Dixon and Baxendale's $\Delta\Delta G_{\text{hyd}}$ estimate for $\text{Ni}^+ \rightarrow \text{Ni}^{2+}$ is 16.5 eV, which is at least 1.5 eV (~ 34 kcal/mol) higher than our DFT-based estimates. The standard deviations estimated for these AIMD $\Delta\Delta G_{\text{hyd}}$ are 0.02 (0.5 kcal/mol) and 0.04 eV (1.0 kcal/mol), respectively. They are calculated by splitting the trajectory in each window into four equal parts, computing the $\Delta\Delta G_{\text{hyd}}$ of each of the four segments, calculating the standard deviation of each, and dividing by $\sqrt{4}$.

Unlike the Li^+ ion, which can be scaled to zero in its entirety,⁵³ transition metal ions carry a substantial amount of d-shell electrons, and AIMD cannot readily be used to yield ΔG_{hyd} .⁵³ The $\Delta\Delta G_{\text{hyd}}$'s are, however, obtained in a

**Figure 5.** $\langle dH(q)/dq \rangle_q$ as a function of q in Ni^{q+} computed using the DFT+ U method. Crosses are for $q \leq 1$, based on configurations generated using AIMD/PBE trajectories, while circles for $q \geq 1$ use snapshots taken from AIMD/DFT+ U trajectories of ref 53. The triangles are test cases that also apply AIMD/DFT+ U to generate trajectories in addition to evaluating $\langle dH(q)/dq \rangle_q$. The results are similar where AIMD/PBE trajectories (crosses) are applied. See text for further discussions.

straightforward manner. AIMD/DFT+ U can be compared to QCT/B3LYP results because the U parameter is fitted to the B3LYP $\text{Ni}^{2+}(\text{H}_2\text{O})_6$ binding energy.

Reasonable agreement is obtained between QCT and AIMD $\Delta\Delta G_{\text{hyd}}$'s, although different approximations are applied. AIMD conducts molecular dynamics sampling of nuclear motion using Newtonian dynamics and does not contain zero-point energies (ZPEs). The QCT approach approximates thermal effects with the harmonic approximation but includes quantum nuclear motion. We have, however, shown that ZPEs contribute minimally, on the order of 0.04 eV (1 kcal/mol), to $\Delta\Delta G_{\text{hyd}}$ (SI). The harmonic approximation is expected to be excellent for rigid hydration structures as in the case with the highly charged, octahedral $\text{Ni}^{2+}(\text{H}_2\text{O})_6$. QCT treats the outer shell water molecules as a dielectric continuum. This does not appear to introduce significant discrepancy.

The AIMD TI calculations are worth examining in more detail. Figure 5 depicts $\langle dH(q)/dq \rangle_q$, which are the integrands in TI for AIMD ΔG_{hyd} as q varies. Despite the large ligand-field splitting and the jumps between the well-defined linear, square-planar, and octahedral hydration structures with the Ni coordinated to two, four, and six H_2O molecules, $\langle dH(q)/dq \rangle_q$ remains reasonably linear, especially for $0.2 \leq q \leq 0.8$ and $1 \leq q \leq 2$. This implies that the six-point trapezoidal discretization is adequate. In fact, a two-point integration scheme already yields a ΔG_{hyd} to within 1 kcal/mol. This behavior seems to be in contrast to an AIMD simulation of the energy gap for $\text{Cu}^+ \rightarrow \text{Cu}^{2+}$, which has been shown to be nonlinear.⁵⁰ The relative lack of curvature in Figure 5 may arise from the exclusion of the bare Ni^{q+} energy. Consequently, $\langle dH(q)/dq \rangle_q$ only reflects hydration effects. The bare Ni^{q+} energy may be the main cause of nonlinearity in ref 50 as q varies because of self-interaction errors in approximate DFT functionals.⁹³ We also stress that $\langle dH(q)/$

dq), the rigorous integrand in TI used here, cannot be treated as vertical reorganization energy. The largest numerical uncertainties occur at the crossover regions where the hydration number changes significantly. For example, the slow fluctuations in N_w for $\text{Ni}^{1.8+}$ (inset to Figure 2) yield the most significant numerical noise in the ΔG_{hyd} integration.

The integrands $\langle dH(q)/dq \rangle_q$ for $q < 1$ and $q > 1$ do not necessarily match at $q = 1$. Their slopes with respect to q also differ. Even in the gas phase, adding or removing a small fractional electron to Ni^+ should yield different results because the electron affinity and ionization potential of Ni^+ differ. As alluded to in section II.C, Wannier function analyses of AIMD snapshots show that all but one value of q used to calculate $\langle dH(q)/dq \rangle_q$ yield a fractional electron localized on Ni. The exception is $q = 0.95$. Recall that $\langle dH(q)/dq \rangle_q$ for this value of q is generated using $q = 1$, which reflects the Ni^+ ion in water. This ion is stable, and no electron delocalization occurs. However, when snapshots along this $q = 1$ AIMD trajectory are taken and q is changed to 0.95 to perform finite difference calculations of $\langle dH(q)/dq \rangle_q$, maximally, Wannier function analysis reveals that the highest occupied molecular orbital containing the fractional (0.05) electron is now centered several Ångströms away from the Ni nucleus. In other words, the $\text{Ni}^{+0.95}/32 \text{ H}_2\text{O}$ simulation actually represents a Ni^+ and an $e^{0.05-}$ delocalized away from the Ni. Therefore, $\langle dH(q)/dq \rangle_q$ for $(q = 1 - \delta q)$ should not be calculated directly, and instead might be extrapolated from smaller q values. Since $\langle dH(q)/dq \rangle_q$ already lies on a straight line with this end point q value, however, performing the extrapolation would not change $\Delta \Delta G_{\text{hyd}}$ significantly, and we have not pursued this avenue.

As discussed above, $\text{Ni}^{(0)}$ is strongly bonded to two H_2O molecules. This makes calculating the singlet $\text{Ni}^{(0)}$ ΔG_{hyd} using the AIMD method difficult because the reference system is the unsolvated triplet $\text{Ni}^{(0)}$. An integration path from that species to $\text{Ni}^{(0)}(\text{H}_2\text{O})_2$ is not readily available. An attempt to use a coordination constraint reaction coordinate⁹⁴ to break $\text{Ni}-\text{H}_2\text{O}$ bonds fails to achieve a sufficient $\text{Ni}-\text{O}_w$ separation such that the subsequent spin-flip energy can be matched to the gas-phase value. As a result, we have relied on QCT to calculate the ΔG_{hyd} of $\text{Ni}^{(0)}$.

Recall that AIMD/PBE and AIMD/DFT+ U trajectories are used to generate the snapshots where $\langle dH(q)/dq \rangle_q$ is computed for $q \leq 1$ and $q \geq 1$, respectively, using the DFT+ U method. In Figure 5, the effect of using AIMD/DFT+ U trajectories (instead of AIMD/PBE ones) is depicted for $q = 0$ and $q = 1$. Using configurations from the former functional yields average $\langle dH(q)/dq \rangle_q$ values that differ by -0.16 and $+0.04$ eV compared to AIMD/PBE configurations for these two q values. (On the scale of the graph, these small differences are almost indistinguishable.) $q = 0$ is expected to give the largest discrepancy because the DFT+ U and PBE methods predict $\text{Ni}^{(0)}(\text{H}_2\text{O})_2$ binding energies that differ the most (by 80%, section III.A). Nevertheless, the hydration structures obtained are sufficiently similar in that snapshots from either type of trajectory can be used to compute $\langle dH(q)/dq \rangle_q$. In the SI, we further show that the $g(r)$ values obtained in AIMD/DFT+ U and AIMD/PBE trajectories are very similar. Since $\Delta \Delta G_{\text{hyd}}$ is obtained by

integrating over the entire range of q , the average of these two values, -0.06 eV or -1.4 kcal/mol, can be taken as an estimate of the small discrepancy in $\Delta \Delta G_{\text{hyd}}$ one can expect if AIMD/DFT+ U were used to generate trajectories throughout.

Finally, we consider the differential hydration free energy between Ni_2 and Ni_2^+ using the QCT method. Table 2 shows that the spin quartet yields $\Delta \Delta G_{\text{hyd}} = -4.42$ eV using the B3LYP functional. These changes in hydration free energies are critical for calculating redox potentials, described in the next subsection.

III.E. Redox Potentials. Estimating the Φ_{redox} of Ni and Ni_2 species requires ionization potentials in addition to $\Delta \Delta G_{\text{hyd}}$. As discussed in our previous work,^{53,54} the first and second IP of Ni are not accurately calculated by either the PBE or B3LYP functional (see the SI). Instead, we adopt the widely accepted experimental values of 7.640 and 18.170 eV for the IPs.^{95,96} Combining the IP and $\Delta \Delta G_{\text{hyd}}$, and subtracting the -4.44 V associated with SHE, the QCT/B3LYP Φ_{redox} for $\text{Ni}^{(0)} \rightarrow \text{Ni}^+$ becomes -2.18 V. The AIMD/DFT+ U Φ_{redox} is a similar value, -2.17 V. These results are consistent with the view that excess electrons (-2.8 V), but not electron-scavenging organic radical anions (-1.2 V), can reduce Ni^+ to a neutral Ni atom dispersed in water.

In contrast, QCT/B3LYP yields $\Phi_{\text{redox}} = -1.05$ V for $\text{Ni}^+ \rightarrow \text{Ni}^{2+}$. This value is within the theoretical uncertainty of the hydroxymethyl radical anion $\Phi_{\text{redox}} = -1.18$ V. (Here, the uncertainty in the predicted value is estimated at ~ 0.2 V, arising from the use of the B3LYP functional for hydration energy compared to CCSD(T).) This suggests that organic radical anions may already be able to reduce Ni^{2+} to Ni^+ in aqueous solutions. AIMD/DFT+ U simulations yield a slightly more negative Φ_{redox} of -1.28 V, which is still reasonably close to the hydroxymethyl radical anion Φ_{redox} .

Our estimate of the Ni^{2+} reduction potential is consistent with the observation that Ni^+ does not appear to reduce Ag^+ to a Ag atom in water.⁹ This suggests that the $\text{Ni}^{2+}(\text{aq})$ one-electron reduction reaction exhibits a Φ_{redox} less negative than the Ag^+ redox reaction reported at -1.75 V versus SHE.⁹ Indeed, the QCT and AIMD estimates of Ni^{2+} Φ_{redox} significantly exceed -1.75 V. Furthermore, in the radiolysis-assisted synthesis of Ni/Pd nanocluster alloys,⁸ the $\text{Pd}^{2+} \rightarrow \text{Pd}^+$ Φ_{redox} is known to exceed -1.18 V, meaning that Pd^{2+} is readily reduced to Pd^+ by organic electron scavengers. If $\text{Ni}^{2+} \rightarrow \text{Ni}^+$ indeed had a Φ_{redox} of -2.7 V,¹⁴ much more negative than -1.18 V, nanoparticle alloy synthesis may seem more difficult to initiate because Pd might have been preferentially nucleated first. But NiPd alloys are indeed observed in experiments.⁸ This observation is arguably more consistent with our revised estimate of Ni^{2+} Φ_{redox} . As discussed in section III.C, in arriving at their -2.7 V estimate for this reduction reaction,¹³ Dixon and Baxendale adopted very different ΔG_{hyd} theoretical estimates. Our modern electronic structure calculations thus yield qualitatively different conclusions compared to earlier calculations reported in the radiolysis literature.

Table 3. Free Energies of Dimerization and Disproportionation Reactions^a

reaction	method	functional	ΔG (eV)
$2\text{Ni}^{(0)} \rightleftharpoons \text{Ni}_2^{(0)}$	QCT	B3LYP	-1.45 eV
$\text{Ni}^+ + \text{Ni}^{(0)} \rightleftharpoons \text{Ni}_2^+$	QCT	B3LYP	-0.41 eV
$2\text{Ni}^+ \rightleftharpoons \text{Ni}^{(0)} + \text{Ni}^{2+}$	QCT	B3LYP	+1.42 eV
	QCT	B3LYP	+1.12 eV*
	AIMD	DFT+U	+1.17 eV*

^a Asterisks indicate that the DFT IPs implicit in the reactions have been replaced by experimental values.

The experimental IP for Ni_2 exhibits extremely large uncertainties.²³ Fortunately, unlike the case of the Ni atom, we find that B3LYP and CCSD(T) yield IP values that are in reasonable agreement with each other (7.73 and 7.42 eV, respectively) when using the 6-311+G(d,p) basis set. This gives us the confidence to adopt the zero temperature CCSD(T) value of 7.42 eV as the N_2 IP. Combined with the ΔG_{hyd} , the B3LYP quasi-chemical Φ_{redox} for reduction of the monovalent nickel dimer, Ni_2^+ becomes -1.44 V. This is lower than the monomeric Ni^+ reduction potential.

III.F. Dimerization and Disproportionation Reactions. Finally, we consider reactions that involve two Ni but no excess electrons (Table 3). Dimerization to form $\text{Ni}_2^{(0)}$ and Ni_2^+ from $\text{Ni}^{(0)}$ and Ni^+ are predicted to be favorable in liquid water. The Ni^+ disproportionation reaction into $\text{Ni}^{(0)}$ and Ni^{2+} is, however, unfavorable. The latter prediction conforms to at least one published experimental result in the literature where Ni atoms are not detected in the presence of Ni^+ (aq).⁹⁷ Ni_2^+ disproportionation into Ni^+ and $\text{Ni}^{(0)}$, the inverse of the second reaction in Table 3, is also unfavorable.

The AIMD results in Table 3 apply the hydration free energies listed in Table 2 and experimental ionization potentials, while the QCT approach implicitly uses B3LYP IP. If experimental IPs are adopted in QCT as well, better quantitative agreement between the AIMD and QCT values is obtained. The qualitative conclusion, however, remains the same: Ni^+ disproportionation remains strongly unfavorable.

Our results in sections III.E and III.F are consistent with the following overall picture. Ni^{2+} is reduced to Ni^+ by solvated electrons and possibly organic radical anions. Ni^+ does not disproportionate into $\text{Ni}^{(0)}$ and Ni^{2+} ; it can, however, be reduced by hydrated excess electrons to $\text{Ni}^{(0)}$. The $\text{Ni}^{(0)}$'s are then immediately consumed to produce larger clusters. These seed clusters become the nuclei of Ni metal nanoparticles.

IV. Conclusions

We have applied first principles methods to calculate the redox potentials (Φ_{redox}) and dimerization free energies of monomeric and dimeric Ni^{q+} species in liquid water. AIMD/DFT and QCT/B3LYP yield Ni^{2+} (aq) one-electron reduction potentials of -1.05 and -1.28 V. These are at least 1.4 V less negative than previous estimates in the radiolysis literature.^{13,14} Φ_{redox} 's predicted from our state-of-the-art electronic structure calculations are within the combined experimental and theoretical uncertainties of the redox potential associated with hydroxymethyl radical anions ($\Phi_{\text{redox}} = -1.18$ V). Our findings suggest that these electron-

scavenging organic species, in addition to hydrated electrons (-2.7 to -2.9 V), may be able to reduce Ni^{2+} to Ni^+ in water. Ni^+ does not readily disproportionate into $\text{Ni}^{(0)}$ and Ni^{2+} .

Even though our calculations are limited to dimers, we can make the following mechanistic prediction. In the beginning, $\text{Ni}^+ + e^- \rightarrow \text{Ni}^{(0)}$ and $\text{Ni}^{2+} + e^- \rightarrow \text{Ni}^+$ readily occurs in γ -irradiated solutions. From the calculated redox potentials (Table 2), the reducing agent is the solvated excess electron in the former case, but the reduction of Ni^{2+} can be accomplished via organic radical anions. In the next step, the reactions $2\text{Ni}^{(0)} \rightarrow \text{Ni}_2^{(0)}$ and $\text{Ni}^+ + \text{Ni}^{(0)} \rightarrow \text{Ni}_2^+$ take place (Table 3, reactions 1 and 2). Even though $\text{Ni}^{(0)}$ can spontaneously undergo a disproportionation reaction with Ni^{2+} to form Ni^+ (Table 3, third reaction), some dimer formation should occur at a sufficient $\text{Ni}^{(0)}$ concentration (i.e., at high radiation dosage). We stress that we have elucidated the thermodynamic feasibility of the reactions but not their relative rates. In γ -radiolysis, the driving force is significant, and the overall reaction may be kinetically limited. These monomers and dimers serve as nuclei for metal nanoparticle growth, yielding larger clusters that coalesce from them. Theoretical studies on these larger clusters will be performed in the future.

Good agreement exists between the quasi-chemical (QCT) method using dielectric continuum approximation for outer-shell hydration contributions and *ab initio* molecular dynamics (AIMD) simulations where outer-shell H_2O molecules are explicitly present. Thus, this study confirms the advantage of using the QCT approach when dealing with transition metal ions with rigid hydration shells.

Acknowledgment. This work was supported by the Department of Energy under Contract DE-AC04-94AL85000, by Sandia's LDRD program. Sandia is a multiprogram laboratory operated by Sandia Corporation, a Lockheed Martin Company, for the U.S. Department of Energy.

Supporting Information Available: Further information is provided regarding ionization potentials, spin splittings, zero temperature binding energies of $\text{Ni}-\text{H}_2\text{O}$ complexes, zero point energy contributions, and more comparison between DFT+U and B3LYP predictions. This information is available free of charge via the Internet at <http://pubs.acs.org/>.

References

- (1) Bartolozzi, M. J. *Power Sources* **1989**, 27, 219.
- (2) Kongolo, K.; Mwema, M. D. *Hyperfine Interact.* **1998**, 111, 281.
- (3) Yamamoto, T.; Liimatainen, J.; Linden, J.; Karppinen, M.; Yamauchi, H. *J. Mater. Chem.* **2000**, 10, 2342.
- (4) Lovell, M. A.; Xie, C.; Xiong, S.; Markesbery, W. R. *J. Alzheimer's Disease* **2003**, 5, 229.
- (5) Desideri, F.; Polticelli, F.; Falconi, M.; Sette, M.; Ciriolo, M. R.; Paci, M.; Rotilio, G. *Arch. Biochem. Biophys.* **1993**, 301, 244.
- (6) Breitenkamp, M.; Henglein, A.; Lilie, J. *Ber. Bunsen. Phys. Chem.* **1976**, 80, 973.

- (7) Zhang, Z. Y.; Nenoff, T. M.; Huang, J.; Berry, D. T.; Provencio, P. *J. Phys. Chem. C* **2009**, *113*, 1155.
- (8) Zhang, Z.; Nenoff, T. M.; Leung, K.; Ferreira, S. R.; Huang, J. Y.; Berry, D. T.; Provencio, P. P.; Stumpf, R. *J. Phys. Chem. C* **2010**, *114*, 14309.
- (9) Ershov, B. G.; Janata, E.; Henglein, A. *J. Phys. Chem.* **1994**, *98*, 7619.
- (10) Belloni, J. *Catal. Today* **2006**, *113*, 141.
- (11) Khatouri, J.; Mostavi, M.; Amblard, J.; Belloni, J. *Z. Phys. D* **1993**, *26*, S82.
- (12) Gachard, E.; Remita, H.; Khatouri, J.; Keita, B.; Nadjio, L.; Belloni, J. *New J. Chem.* **1998**, 1257.
- (13) Baxendale, J. H.; Dixon, R. S. *Z. Phys. Chem. (Munich)* **1964**, *43*, 161.
- (14) Baxendale, J. H.; Keene, J. P.; Scott, D. A. *Chem. Commun.* **1966**, *20*, 715.
- (15) Ershov, B. G. *Russ. Chem. Bull.* **1999**, *48*, 1.
- (16) Jacobson, D. B.; Freiser, B. S. *J. Am. Chem. Soc.* **1986**, *108*, 27.
- (17) Klotzbuecher, W.; Ozin, G. A. *Inorg. Chem.* **1977**, *16*, 984.
- (18) Koretsky, G. M.; Kerns, K. P.; Nieman, G. C.; Knickelbein, M. B.; Riley, S. J. *J. Phys. Chem. A* **1999**, *103*, 1997.
- (19) Sun, Y.; Fournier, R.; Zhang, M. *Phys. Rev. A* **2009**, *79*, 043202.
- (20) Ershov, B. G.; Janata, E.; Henglein, A.; Fotjik, A. *J. Phys. Chem.* **1993**, *97*, 4589.
- (21) Janata, E.; Henglein, A.; Ershov, B. G. *J. Phys. Chem.* **1994**, *98*, 10888.
- (22) Zhao, Y.; Truhlar, D. G. *J. Chem. Phys.* **2006**, *125*, 194101.
- (23) Rohlfing, E. A.; Cox, D. M.; Kaldor, A. *J. Phys. Chem.* **1984**, *88*, 4497.
- (24) Michelini, M. C.; Diez, R. P.; Jubert, A. H. *Comput. Mater. Sci.* **2004**, *31*, 292.
- (25) Merchan, M.; Pou-Amerigo, R.; Roos, B. O. *Chem. Phys. Lett.* **1996**, *252*, 405.
- (26) Reddy, B. V.; Nayak, S. K.; Khanna, S. N.; Rao, B. K.; Jena, P. *J. Phys. Chem. A* **1998**, *102*, 1748.
- (27) Andrés Cisneros, G.; Castro, M.; Salahub, D. R. *Int. J. Quantum Chem.* **1999**, *75*, 847.
- (28) Knickelbein, M. B.; Yang, S.; Riley, S. J. *J. Chem. Phys.* **1990**, *93*, 94.
- (29) Arvizu, G. L.; Calaminici, P. *J. Chem. Phys.* **2007**, *126*, 194102.
- (30) Belloni, J.; Mostafavi, M.; Remita, H.; Marignier, J. L.; Delcourt, M. O. *New J. Chem.* **1998**, *22*, 1239.
- (31) Henglein, A.; Meisel, D. *Langmuir* **1998**, *14*, 7392.
- (32) Wardman, P. *J. Phys. Chem. Ref. Data* **1989**, *18*, 1637.
- (33) Baxendale, J. H. *Radiat. Res. Suppl.* **1964**, *4*, 114.
- (34) Noyes, R. M. *J. Am. Chem. Soc.* **1962**, *84*, 513.
- (35) Asthagiri, D.; Pratt, L. R.; Paulaitis, M. E.; Rempe, S. B. *J. Am. Chem. Soc.* **2004**, *126*, 1285.
- (36) Li, J.; Fisher, C. L.; Chen, J. L.; Bashford, D.; Noodleman, L. *Inorg. Chem.* **1996**, *35*, 4694.
- (37) Roy, L. E.; Jakubikova, E.; Guthrie, M. G.; Batista, E. R. *J. Phys. Chem. A* **2009**, *113*, 6745.
- (38) Galstyan, A.; Knapp, E. W. *J. Comput. Chem.* **2009**, *30*, 203.
- (39) Tsushima, S. *J. Phys. Chem. B* **2008**, *112*, 13059.
- (40) Uudsemaa, M.; Tamm, T. *J. Phys. Chem. A* **2003**, *107*, 9997.
- (41) Jaque, P.; Marenich, A. V.; Cramer, C. J.; Truhlar, D. G. *J. Phys. Chem. C* **2007**, *111*, 5783.
- (42) Baik, M.; Friesner, R. A. *J. Phys. Chem. A* **2002**, *106*, 7407.
- (43) Sabo, D.; Varma, S.; Martin, M. G.; Rempe, S. B. *J. Phys. Chem. B* **2008**, *112*, 867.
- (44) Varma, S.; Rempe, S. B. *J. Am. Chem. Soc.* **2008**, *130*, 15405.
- (45) Asthagiri, D.; Dixit, P. D.; Merchant, S.; Paulaitis, M.; Pratt, L. R.; Rempe, S. B.; Varma, S. *Chem. Phys. Lett.* **2010**, *485*, 1.
- (46) Pratt, L. R.; LaViolette, R. A. *Mol. Phys.* **1998**, *94*, 909. Pratt, L. R.; Rempe, S. B. *Simulation and Theory of Electrostatic Interactions in Solution*; Pratt, L. R., Hummer, G., Eds.; AIP: New York, 1999; pp 172–201. Beck, T. L.; Paulaitis, M. E.; Pratt, L. R. *The Potential Distribution Theorem: Models of Molecular Solutions*; Cambridge University Press: New York, 2006; pp 166–195. Pratt, L. R.; Asthagiri, D. *Free Energy Calculations*; Chipot, C., Pohorille, A., Eds.; Springer-Verlag: Berlin, 2007; pp 323–352.
- (47) See, e.g.: Swift, T. J.; Connick, R. E. *J. Chem. Phys.* **1962**, *37*, 307. The exchange of water molecules in the Ni^{2+} first hydration shell with bulk water was estimated to occur on 10 ps timescales. We did not observe such exchanges when generating the Ni^{2+} (aq) trajectory in ref 53. However, we adopted deuterium mass for protons and used a thermostat; therefore, the AIMD dynamics cannot be directly compared with experimental timescales.
- (48) Blumberger, J.; Sprik, M. *J. Phys. Chem. B* **2004**, *108*, 6529.
- (49) Blumberger, J.; Tateyama, Y.; Sprik, M. *Comput. Phys. Commun.* **2005**, *169*, 256.
- (50) Blumberger, J. *J. Am. Chem. Soc.* **2008**, *130*, 16065.
- (51) VandeVondele, J.; Ayala, R.; Sulpizi, M.; Sprik, M. *J. Electroanal. Chem.* **2007**, *607*, 113. Tateyama, Y.; Blumberger, J.; Ohno, T.; Sprik, M. *J. Chem. Phys.* **2007**, *126*, 204506.
- (52) Kollman, P. A. *Chem. Rev.* **1983**, *93*, 2395.
- (53) Leung, K.; Rempe, S. B.; von Lilienfeld, O. A. *J. Chem. Phys.* **2009**, *130*, 204507.
- (54) Rempe, S. B.; Leung, K. *J. Chem. Phys.* **2010**, *133*, 047104.
- (55) Rempe, S. B.; Pratt, L. R.; Hummer, G.; Kress, J. D.; Martin, R. L.; Redondo, A. *J. Am. Chem. Soc.* **2000**, *122*, 966. Rempe, S. B.; Pratt, L. R. *Fluid Phase Equilib.* **2001**, *183*, 121. Rempe, S. B.; Asthagiri, D.; Pratt, L. R. *Phys. Chem. Chem. Phys.* **2004**, *6*, 1966.
- (56) Varma, S.; Rempe, S. B. *Biophys. J.* **2007**, *93*, 1093.
- (57) Varma, S.; Sabo, D.; Rempe, S. B. *J. Mol. Biol.* **2008**, *376*, 13.
- (58) Pasquarello, A.; Petri, I.; Salmon, P. S.; Parisel, O.; Car, R.; Toth, E.; Powell, D. H.; Fischer, H. E.; Helm, L.; Merbach, A. E. *Science* **2001**, *291*, 856.
- (59) Bernasconi, L.; Blumberger, J.; Sprik, M.; Vuilleumier, R. *J. Chem. Phys.* **2004**, *121*, 11885. Sherman, D. M. *Geochim. Cosmochim. Acta* **2007**, *71*, 714.
- (60) Schwenk, C. F.; Rode, B. M. *Chem. Phys. Chem.* **2003**, *4*, 931.
- (61) Schwenk, C. F.; Rode, B. M. *J. Chem. Phys.* **2003**, *119*, 9523. Blumberger, J.; Bernasconi, L.; Tavernelli, I.; Vuilleumier, R.; Sprik, M. *J. Am. Soc. Chem.* **2004**, *126*, 3928.

- (62) Anisimov, V. I.; Zaanen, J.; Andersen, O. K. *Phys. Rev. B* **1991**, *44*, 943. Liechtenstein, A. I.; Anisimov, V. I.; Zaanen, J. *Phys. Rev. B* **1995**, *52*, 5467.
- (63) The DFT+U implementation in VASP was described in: Rohrbach, A.; Hafner, J.; Kresse, G. *Phys. Rev. B* **2004**, *69*, 075413.
- (64) Kulik, H. J.; Cococcioni, M.; Scherlis, D. A.; Marzari, N. *Phys. Rev. Lett.* **2006**, *97*, 103001. Scherlis, D. A.; Cococcioni, M.; Sit, P. H. L.; Marzari, N. *J. Phys. Chem. B* **2007**, *111*, 7384. Sit, P. H. L.; Cococcioni, M.; Marzari, N. *J. Electroanal. Chem.* **2007**, *607*, 107. Leung, K.; Rempe, S. B.; Schultz, P. A.; Sproviero, E. M.; Batista, V. S.; Chandross, M. E.; Medforth, C. J. *J. Am. Chem. Soc.* **2006**, *128*, 3659. Leung, K.; Medforth, C. J. *J. Chem. Phys.* **2007**, *126*, 024501. Leung, K.; Nielsen, I. M. B.; Sai, N.; Medforth, C. J.; Shelnutt, J. A. *J. Phys. Chem. A* **2010**, *114*, 10174. Panchmatia, P. M.; Sanyal, B.; Oppeneer, P. M. *Chem. Phys.* **2008**, *343*, 47. Oppeneer, P. M.; Panchmatia, P. M.; Sanyal, B.; Eriksson, O.; Ali, M. E. *Prog. Surf. Sci.* **2009**, *84*, 18.
- (65) Frisch, M. J.; Trucks, G. W.; Schlegel, H. B.; Scuseria, G. E.; Robb, M. A.; Cheeseman, J. R.; Scalmani, G.; Barone, V.; Mennucci, B.; Petersson, G. A.; Nakatsuji, H.; Caricato, M.; Li, X.; Hratchian, H. P.; Izmaylov, A. F.; Bloino, J.; Zheng, G.; Sonnenberg, J. L.; Hada, M.; Ehara, M.; Toyota, K.; Fukuda, R.; Hasegawa, J.; Ishida, M.; Nakajima, T.; Honda, Y.; Kitao, O.; Nakai, H.; Vreven, T.; Montgomery, J. A., Jr.; Peralta, J. E.; Ogliaro, F.; Bearpark, M.; Heyd, J. J.; Brothers, E.; Kudin, K. N.; Staroverov, V. N.; Kobayashi, R.; Normand, J.; Raghavachari, K.; Rendell, A.; Burant, J. C.; Iyengar, S. S.; Tomasi, J.; Cossi, M.; Rega, N.; Millam, N. J.; Klene, M.; Knox, J. E.; Cross, J. B.; Bakken, V.; Adamo, C.; Jaramillo, J.; Gomperts, R.; Stratmann, R. E.; Yazyev, O.; Austin, A. J.; Cammi, R.; Pomelli, C.; Ochterski, J. W.; Martin, R. L.; Morokuma, K.; Zakrzewski, V. G.; Voth, G. A.; Salvador, P.; Dannenberg, J. J.; Dapprich, S.; Daniels, A. D.; Farkas, Ö.; Foresman, J. B.; Ortiz, J. V.; Cioslowski, J.; Fox, D. J. *Gaussian*; Gaussian, Inc.: Wallingford, CT, 2009.
- (66) Pople, J. A.; Head-Gordon, M.; Raghavachari, K. *J. Chem. Phys.* **1987**, *87*, 5968. Purvis, G. D.; Bartlett, R. J. *J. Chem. Phys.* **1993**, *76*, 1910.
- (67) Becke, A. D. *J. Chem. Phys.* **1993**, *98*, 1372. Becke, A. D. *J. Chem. Phys.* **1993**, *98*, 5648. Lee, C. T.; Yang, W. T.; Parr, R. G. *Phys. Rev. B* **1988**, *37*, 785.
- (68) Perdew, J. P.; Burke, K.; Ernzerhof, M. *Phys. Rev. Lett.* **1996**, *77*, 3865.
- (69) Stefanovich, E. V.; Truong, T. N. *Chem. Phys. Lett.* **1995**, *244*, 65.
- (70) Ohtaki, H.; Radnai, T. *Chem. Rev.* **1993**, *93*, 1157.
- (71) Bol, W.; Gerrits, G. J.; Panthale, C. L. *J. Appl. Crystallogr.* **1970**, *3*, 486.
- (72) Baker, N. A.; Sept, D.; Joseph, S.; Holst, M. J.; McCammon, J. A. *Proc. Natl. Acad. Sci. U. S. A.* **2001**, *98*, 10037.
- (73) Bank, R.; Holst, M. *Soc. Ind. Appl. Math. J. Sci. Comput.* **2000**, *22*, 1411.
- (74) Kresse, G.; Furthmüller, J. *Phys. Rev. B* **1996**, *54*, 11169. Ibid. *Comput. Mater. Sci.* **1996**, *6*, 15.
- (75) Blöchl, P. E. *Phys. Rev. B* **1994**, *50*, 17953. 1994.
- (76) The VASP implementation is discussed in: Kresse, G.; Joubert, D. *Phys. Rev. B* **1999**, *59*, 1758.
- (77) Cramer, C. J.; Truhlar, D. G. *Phys. Chem. Chem. Phys.* **2009**, *11*, 10757.
- (78) Schultz, N. E.; Zhao, Y.; Truhlar, D. G. *J. Phys. Chem. A* **2005**, *109*, 4388, and references therein.
- (79) Schwegler, E.; Grossman, J. C.; Gygi, F.; Galli, G. *J. Chem. Phys.* **2004**, *121*, 5400. Sit, P. H.-L.; Marzari, N. *J. Chem. Phys.* **2005**, *122*, 204510. Rempe, S. B.; Mattsson, T. R.; Leung, K. *Phys. Chem. Chem. Phys.* **2008**, *10*, 4685.
- (80) Berendsen, H. J. C.; Grigera, J. R.; Straatsma, T. P. *J. Phys. Chem.* **1987**, *91*, 6269.
- (81) Nobuyuki, O.; Christopher, S.; Sapan, A. S.; Marcos, M. G.; Axel, T. B. *Proteins: Struct., Funct., Genet.* **1999**, *37*, 641.
- (82) Leung, K.; Marsman, M. *J. Chem. Phys.* **2007**, *127*, 154722.
- (83) Hummer, G.; Pratt, L. R.; Garcia, A. E. *J. Phys. Chem.* **1996**, *100*, 1206.
- (84) Hummer, G.; Pratt, L. R.; Garcia, A. E. *J. Chem. Phys.* **1997**, *107*, 9275.
- (85) Marzari, N.; Vanderbilt, D. *Phys. Rev. B* **1997**, *56*, 12847.
- (86) Pratt, L. R. *J. Phys. Chem.* **1992**, *96*, 25. Wilson, M. A.; Pohorille, A.; Pratt, L. R. *J. Chem. Phys.* **1989**, *90*, 5211. Wilson, M. A.; Pohorille, A.; Pratt, L. R. *J. Phys. Chem.* **1987**, *91*, 4873. Sokhan, V. P.; Tildesley, D. J. *Mol. Phys.* **1997**, *it*, 625.
- (87) Leung, K. *J. Phys. Chem. Lett.* **2010**, *1*, 496.
- (88) Jackson, J. D. *Classical Electrodynamics*; Wiley: New York, 1999; Chapter 2.
- (89) Orgel, L. E. *An Introduction to Transition-Metal Chemistry: Ligand-Field Theory*; Methuen & Co.: London, 1960; pp 46.
- (90) Mulliken, R. S. *J. Chem. Phys.* **1955**, *23*, 1833. Stone, A. J. *Chem. Phys. Lett.* **1981**, *83*, 233.
- (91) Zhang, F. S.; Lynden-Bell, R. M. *Phys. Rev. Lett.* **2003**, *90*, 185505.
- (92) Marcus, Y. *Biophys. Chem.* **1994**, *51*, 111.
- (93) See, e.g.: Mori-Sánchez, P.; Cohen, A. J.; Yang, W. T. *J. Chem. Phys.* **2006**, *125*, 201102.
- (94) Sprik, M. *Chem. Phys.* **2000**, *258*, 139.
- (95) Balabanov, N. B.; Peterson, K. A. *J. Chem. Phys.* **2006**, *125*, 074110.
- (96) Shenstone, A. G. *J. Res. Natl. Bur. Stand. (U.S.)* **1970**, *74A*, 80.
- (97) Kelm, M.; Lilie, J.; Henglein, A.; Janata, E. *J. Phys. Chem.* **1974**, *78*, 882.